Thin Solid Films 606 (2016) 120–126

Contents lists available at ScienceDirect

Thin Solid Films

journal homepage: www.elsevier.com/locate/tsf

Investigation of phase transformation for ferrite–austenite structure in stainless steel thin films

Noureddine Merakeb [a], Amel Messai [b], Ahmad I. Ayesh [c,*]

[a] Laboratory of Physical Metallurgy and Property of Materials (LM2PM), Metallurgy and Materials Engineering Department, Badji Mokhtar University, P.O. Box 12, Annaba 23000, Algeria
[b] Laboratoire d'Ingénierie et Sciences des Matériaux Avancés (ISMA), Institut des Sciences et Technologie, Abbès Laghrour University, Khenchela 40000, Algeria
[c] Department of Mathematics, Statistics and Physics, Qatar University, Doha, Qatar

ARTICLE INFO

Article history:
Received 16 February 2016
Received in revised form 13 March 2016
Accepted 20 March 2016
Available online 22 March 2016

Keywords:
Ferrite–austenite
Stainless steel
Thin film
Thermal evaporation

ABSTRACT

In this work we report on phase transformation of 304 stainless steel thin films due to heat treatment. Ex-situ annealing was applied for evaporated 304 stainless steel thin films inside an ultra-high vacuum chamber with a pressure of 3×10^{-7} Pa at temperatures of 500 °C and 600 °C. The structure of thin films was studied by X-ray diffraction (XRD) and conversion electron Mössbauer spectroscopy (CEMS) techniques. The results revealed a transformation from α-phase that exhibits a body-centered cubic structure (BCC) to γ-phase that exhibits a face-centered cubic (FCC) due to annealing. In addition, the percentage of γ-phase structure increased with the increase of annealing temperature. Annealing thin films increased the crystal size of both phases (α and γ), however, the increase was nonlinear. The results also showed that phase transformation was produced by recrystallization of α and γ crystals with a temporal evolution at each annealing temperature. The texture degree of thin films was investigated by XRD rocking curve method, while residual stress was evaluated using curvature method.

1. Introduction

Stainless steel is a highly demanded material in different fields due to its wide range of industrial applications in fields such as chemical processing, oil and gas, food production, and power generation [1–3] due to its outstanding mechanical properties as well as resistance to corrosion [4–6]. In the last decades, many investigations were carried out to study structural modification of 304 stainless steel films fabricated by sputtering technique, where the sputtering target is normally made of 304 stainless steel of γ-phase [7–9]. It was reported that the structure of these sputtered films contains both phases: γ and α [10]. Herein, if stainless steel films are generated by sputtering at a substrate temperature between 375 °C and 500 °C, they are likely to develop a structure that contains both phases [11–13]. If the sputtered 304 stainless steel films are formed on substrates at room temperature, they can develop a structure constitute by both phases. The α-phase in those films is an unstable phase, due to rapid quenching of the sputtered atoms and small clusters when they are deposited on a substrate at room temperature [14].

α-Phase in sputtered stainless steel thin films was reported to undergo a transformation to γ-phase at 477 °C [15] because α-phase is unstable at 477 °C or above. In addition, it was also observed that a full $\alpha \rightarrow \gamma$ phase transformation occurs at 677 °C for the above thin films. It should be noted here that sputtered 304 stainless steel thin films that are fabricated at room temperature are ferromagnetic due to the majority of α-phase [7] unlike bulk 304 stainless steel which is a non-magnetic material [16]. In addition, the transformation temperature of sputtered stainless steel thin films from α-phase to γ-phase is defined as Curie temperature, which is about 600 °C [7]. Beyond this temperature sputtered thin films would have a full phase transformation to γ-phase and they become non-magnetic similar to bulk 304 stainless steel [16].

Recently, we used the thermal evaporation method to prepare 304 stainless steel thin films [17,18]. It was demonstrated that the evaporated 304 stainless steel thin films exhibit nanocrystals ferrite–austenite mixture structure with a ratio of 6% for the γ-phase. In this work, the structural modification of ferrite–austenite mixture of 304 stainless steel thin films fabricated by thermal evaporation due to heat treatment is investigated by XRD and CEMS. Thin film stress is determined using the curvature method.

2. Experimental

2.1. Thin film preparation

Stainless steel thin films were deposited on quartz substrates with a thickness of 166 nm inside a high vacuum chamber by thermal evaporation, and used to investigate phase transformation. The thickness of the films was measured using a quartz crystal monitor placed close to the substrates. The details of the fabrication method were described elsewhere [17]. Table 1 presents the fabrication conditions. Thin films of

---

* Corresponding author.
E-mail address: ayesh@qu.edu.qa (A.I. Ayesh).

http://dx.doi.org/10.1016/j.tsf.2016.03.038
0040-6090/

Table 1
Conditions of thin film preparation.

Thin film fabrication conditions	
Distance between substrate and crucible	20 cm
Residual pressure in deposition chamber	10^{-4} Pa
Evaporation temperature of 304 SS bulk	1400 °C
Substrate temperature during deposition	25 °C
Deposition speed of 304 SS thin films	10.3 nm/s

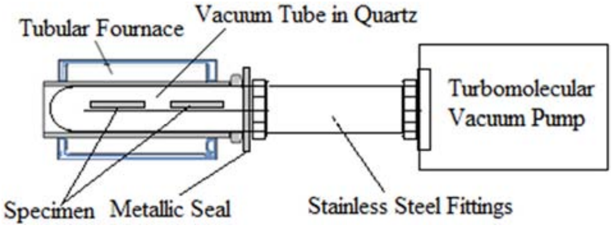

Fig. 1. Description of annealing system and its components.

different thicknesses were also prepared on silicon substrates and used to study residual stress of thin films.

2.2. Thin film annealing

Ex-situ annealing for thin films was carried out at 500 °C and 600 °C in an ultra-high vacuum chamber at 3×10^{-7} Pa placed inside a tube furnace for 1 h at each temperature. Figure 1 shows a schematic diagram of the annealing system that employed a turbo-molecular pump to achieve such a high vacuum. The annealing temperatures were chosen to cover the temperature range of phase transition. Quartz substrates were utilized since they are mechanically adequate for heat treatments, and they permit realization of annealing without atomic diffusion at the interface between thin films and substrate. The ultra-high vacuum ensured avoiding sample contamination or oxidation during the annealing. Furthermore, annealing and cooling rates of thin films were sufficiently slow to prevent their deterioration due to temperature gradient effect.

2.3. Characterization

2.3.1. XRD

X-ray diffraction (XRD) analyses of stainless steel thin films were performed using a SIEMENS D500/501 diffractometer using Cu-K_α radiation ($\lambda = 1.5406$ Å). XRD data were collected for 2θ in the range of 40°–140°. The diffractometer was equipped with a graphite monochromator placed before the detector to eliminate K_β radiation.

2.3.2. X-ray diffraction rocking curve method

The texture degree of thin films annealed at 500 °C for 1 h has been determined by X-ray diffraction rocking curve method [19–21]. Herein, the rocking curve method was applied to the (110) peak of α-phase taken from the X-ray diagram. A Lorentzian fit was applied to the (110) peak and the parameters are given in Table 2, where it is noted that the (110) peak corresponds to $2\theta = 44.80°$ (i.e. $\theta = 22.40°$).

In X-ray diffraction rocking curve method, X-ray source and detector were fixed in a position that corresponds to 2θ of Bragg's peak (110).

Table 3
Chemical composition of stainless steel thin film and the initial bulk material.

Chemical composition (wt.%)						
Elements	Fe	Cr	Ni	Mn	Si	C
304 SS thin films	71.75	17.06	7.60	3.48	–	–

The sample was rotated with an angle (Ω) about an axis perpendicular to the focal plane crossing an adjusted angular space at θ. In this experiment, Ω was varied from 2° to 42° with a step size of 0.5°, where this step size permitted to define the disorientation degree of diffraction planes relative to thin films surface. The maximum of the peak her is θ. The full-width at half maximum (FWHM) of the rocking curve peak was determined after the Lorentzian fit which permits to estimate the texture degree of the produced thin films.

2.3.3. Residual stress

The curvature method was utilized for determination of thin film's stress based on the change of curvature of silicon substrate (Si-(100)) of deposited thin film. Silicon substrate of high elasticity of 180.5 GPa [22], and dimensions of 200 μm (thickness) × 0.3 mm (width) were used for this study.

304 stainless steel thin films with thicknesses of 110, 120, 133, and 166 nm, were deposited on the substrates and used to study the influence of thickness and annealing on stress. The 166 nm thick film was annealed at 500 °C for 1 h and used to study the effect of annealing on stress. Fabrication and annealing conditions of thin films deposited on silicon substrate were similar to those deposited on quartz substrates above.

The application of curvature method is based on the measurement of the curvature size (R) that results from substrate bend (f) and the substrate length (L). The radius of curvature can be calculated using [23]:

$$R = \left(\frac{f}{2} + \frac{L^2}{8f}\right) \tag{1}$$

Eq. (1) expresses the geometrical relationship between R, L, and f of the curvature for a silicon substrate. It should be noted her that (f/2) is very small compared with $(\frac{L^2}{8\,f})$, thus, it can be ignored.

L and f were measured in this work using a mechanical profilometer: DEKTAK II. The measurements of both quantities were carried out before and after thin film deposition and treatment. L was 8 mm for all samples. Furthermore, measurements were carried out in both directions along the length of each substrate eight times per sample to reduce the error of manipulation. The stress can be calculated for a thin film by Stoney's relation [24]:

$$\sigma = \left(\frac{E}{1-\nu}\right)_S \left(\frac{H_s^2}{6h_f}\right) \left(\frac{1}{R} - \frac{1}{R_0}\right) \tag{2}$$

where E and ν are substrate's Young's modulus and Poisson's ratio, respectively, $(E/(1-\nu))_s$ is the term that expresses the elasticity of the substrate and it is equal to 180.5 GPa, and H_s and h_f are the thicknesses of substrate and thin film, respectively.

Table 2
Parameters of the fitting for the peaks: (110) α-phase and (111) γ-phase.

Diffraction peaks	Non-annealing		Annealing: 1 h—500 °C		Annealing: 1 h—600 °C	
	FWHM (°)	Intensities ratios I_γ/I_α	FWHM (°)	Intensities ratios I_γ/I_α	FWHM (°)	Intensities ratios I_γ/I_α
(111)-γ $2\theta = 43.85°$	1.13	0.0424	0.2447	0.5125	0.2502	0.7015
(110)-α $2\theta = 44.80°$	0.55		0.2787		0.3033	

2.3.4. CEMS

Conversion electron Mössbauer spectroscopy (CEMS) was recorded using a constant acceleration spectrometer at room-temperature with a 57-Co/Rh source (50 mCi) and a continuous gas flow proportional counter (using He and 5% CH_4 gases at 293 K). The Mössbauer technique enabled examining atomic coordination in the neighborhood of probe nuclei via hyperfine interaction parameters. The spectra were computer fitted which yielded the hyperfine magnetic field (HMF) distribution, where it was assumed that each spectrum is superposition of number of sub-spectra having different hyperfine interactions and relative contributions. In all cases, the isomer shift at the 57-Fe, nucleus is given relative to α-Fe at room temperature.

2.3.5. SEM/EDX

A JEOL 5600-2v scanning electron microscope (SEM) was utilized to investigate the morphology of the produced thin films using an accelerating voltage of 20 kV. The composition of thin films was also determined by an energy-dispersive X-ray spectroscopy (EDX) system attached to the SEM. Table 3 shows the composition of the fabricated thin films. The table reveals a relativly high concentration of Mn which can be assigned to its high evaporation rate [25].

3. Results and discussion

3.1. Surface analysis

The surface morphology of annealed thin films is investigated by SEM as shown in Fig. 2. The image reveals that the film is free of apparent defects or microscopic cracks, and it exhibits a homogeneous and regular texture. In addition, the micrograph shows that the annealed thin film is clean which indicates that annealing under vacuum is suitable to prevent contamination during annealing process.

3.2. Structure analysis

3.2.1. XRD analysis

Structural modifications of thin films due to heat treatments are investigated using XRD analysis and presented in Fig. 3. The figure reveals the XRD measurements of three thin films: as-grown, annealed at 500 °C, and annealed at 600 °C. The results are analyzed using PDF-JCPDS cards 6–696 and 33–397, and the (110) α-phase of body-centered cubic structure (BCC) as well as the (111) γ-phase of face-centered cubic (FCC) are identified. XRD results of as-grown thin film show the peaks of α-phase: (110) and (211), where the (110) peak has high intensity which indicates that the as-grown thin films exhibit good crystallinity. The (111) peak of γ-phase appears with very low intensity which indicates the low percentage of γ-phase within the as-grown thin films. XRD measurements of the thin film annealed at 500 °C show two peaks that belong to γ-phase: (111) and (200), with a clear increase in the intensity of the (111) peak (compared to that of the as-grown film). Furthermore, an increase in the intensity of α-phase peak (110) compared to that of the as-grown film is observed. XRD results of thin films annealed at 600 °C show the disappearance of the (211) peak of α-phase, increase in the intensities of the (111) and (200) peaks of γ-phase, and a decrease in the intensity of the (110) peak of α-phase. It is well established that the increase in the intensity of XRD peaks that corresponds to a particular crystal structure is due to the increase in the percentage of that structure [26]. The above XRD results reveal the evolution of the minority γ-phase due to annealing of the thin films. This also demonstrates that the percentage of the minority γ-phase crystals increases compared to the majority α-phase

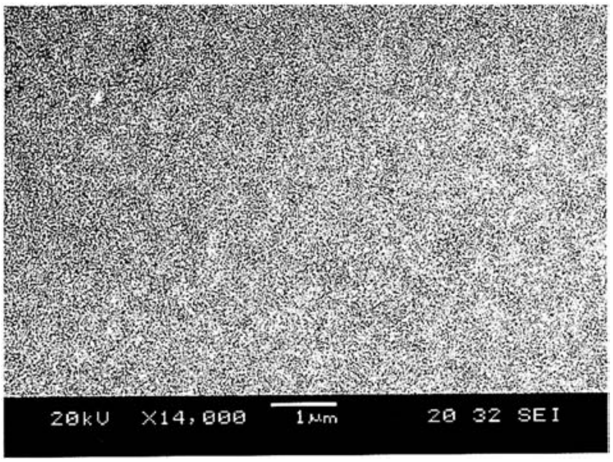

Fig. 2. SEM micrograph of annealed 304 stainless steel thin film (1 h at 600 °C).

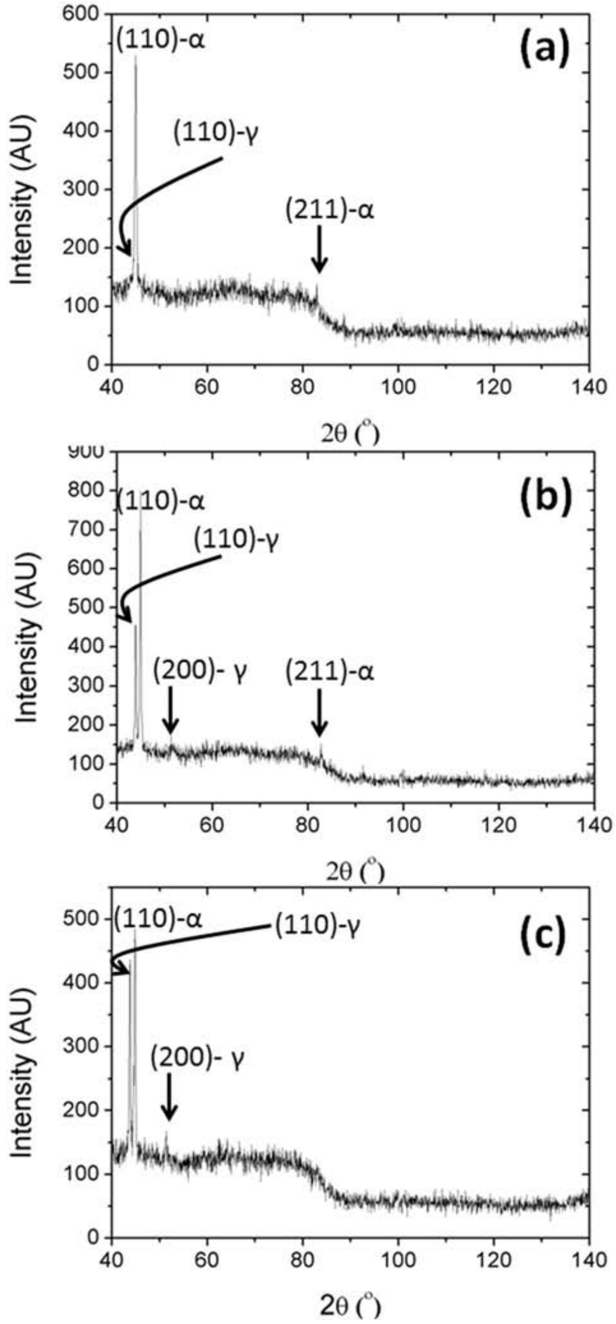

Fig. 3. XRD diagrams of the 304 stainless steel thin films on quartz. (a) As-grown, (b) annealed at 500 °C, and (c) annealing at 600 °C. Annealing time is 1 h.

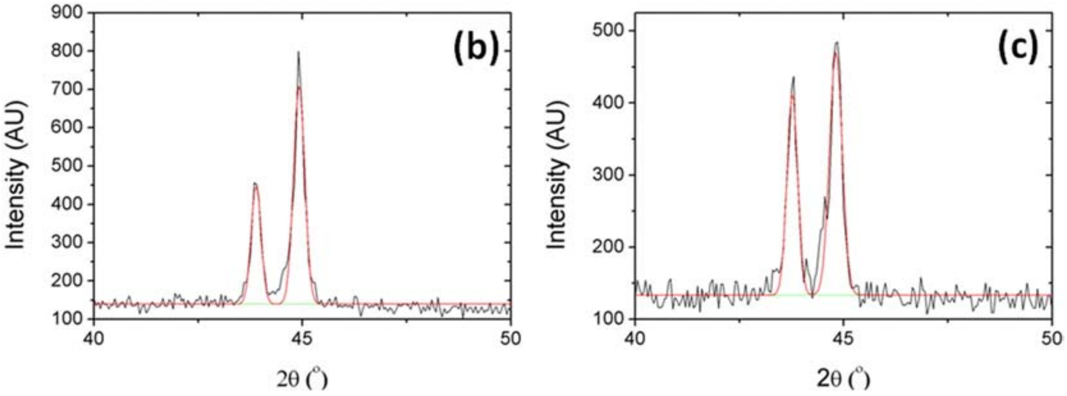

Fig. 4. Fitting by Pseudo-Voigt model of (110) α-phase and (111) γ-phase taken from the XRD patterns of Fig. 4(b) and 4(c) that are annealed for 1 h at 500 °C and 600 °C, respectively.

crystals with temperature. Therefore, it can be concluded that the as-grown stainless steel thin films fabricated by thermal evaporation exhibit a metastable structure that contains both phases: α and γ phases, and the α-phase undergoes a partial transformation into γ-phase due to annealing [27].

3.2.1.1. Quantifying phase transformation. The main peaks in the XRD patterns ((111) for γ-phase and (110) for α-phase) are fitted by means of Pseudo-Voigt model to quantify the ratio of both phases. Figure 4 shows the fit result of both peaks. The fitting parameters and results are presented in Table 2.

Quantitative phases analysis can be performed using the intensity ratio (I_γ/I_α) which is proportional to the volume fraction ratio of the corresponding phase (C_γ/C_α) and the ratio of the characteristic coefficient of the considered phases (R_γ/R_α) using [26,28]:

$$\frac{I_\gamma}{I_\alpha} = \frac{C_\gamma}{C_\alpha}\frac{R_\gamma}{R_\alpha} \tag{3}$$

where, R depends on the angle θ and type of material, and its calculation requires knowledge of the crystal structure and lattice parameters of both phases. The calculation results that correspond to both diffraction peaks: (111) of γ-phase and (110) of α-phase are presented in Tables 2 and 4. Table 4 reveals that as-grown thin films contain 94% of α-phase and 6% of γ-phase, thin films that are annealed at 500 °C contain 59% of α-phase and 41% of γ-phase, and thin films that are annealed at 600 °C contain 51% of α-phase and 49% γ-phase. These results are in good agreement with those obtained for sputtered 304 stainless steel thin films after annealing at 700 °C which present a complete transformation of α-phase to γ-phase [29].

3.2.1.2. Crystal size. The crystal size can be estimated from XRD measurements using Scherrer's equation [26]:

$$\mathrm{D} = \frac{\mathrm{K}\lambda}{\beta \cos\theta} \tag{4}$$

where D is the average diameter of a crystal, θ is Bragg's angle, β is FWHM of the diffracted peak at 2θ, λ is the incidental wavelength of Cu-K$_\alpha$ = 1.54056 Å, and K is a constant that depends on crystal shape. In the present study K = 1 was used because the grains do not have a specific shape.

Eq. (4) was used to calculate the crystal size using the (110) of α-phase and (111) of γ-phase, and the results are shown in Table 5. The table reveals that for as-grown thin films, α crystals are twice as large as γ crystals. Annealing thin films at 500 °C causes a sharp increase in the crystal size of both α and γ phases. However, increasing the annealing temperature to 600 °C causes a slight decrease in the crystal size of α-phase while the size of γ-phase crystals remains unchanged.

Nevertheless, crystals of annealed thin films for α and γ phases are almost analogous in size. In addition, the growth rate of crystal size is greater for γ-phase compared with that of α-phase when thin films are annealed at 500 °C. Therefore, annealing those stainless steel thin films causes nonlinear growth of crystal size for both α and γ crystals. The obtained results demonstrate that α → γ phase transformation is produced by the recrystallization phenomena (germination and germ growth) with temporal evolution at each annealing temperature which is given by the Johnson–Mehl–Avrami (JMA) law [30]:

$$c \;=\; 1-\; e^{-(\delta t)^n} \tag{5}$$

where c is the phase fraction, n is the Avrami exponent, t is the annealing time, and δ is the kinetics constant. This equation describes heterogeneous germination, where α and γ crystals develop simultaneously with time during annealing. In addition, the germination rates of α and γ crystals, are inversely proportional. Those results are in agreement with results published for stainless steel thin films fabricated by sputtering [10,31].

3.2.2. X-ray diffraction rocking curve method

The (110) diffraction peak of α-phase in Fig. 3(b) was chosen to estimate the texture degree because it corresponds to the majority phase in the films. The results of the rocking curve peak fitted by Lorentzian distribution are presented in Fig. 5. The figure shows the pattern obtained by Ω-scan around θ = 22.4° that corresponds to the peak edge which is considered as the axis of the peak. The FWHM is 15.65°, and it is dominated by the disorientation of the majority α-phase crystals of the

Table 4
Abundance of α and γ phases.

304 SS thin films state	Intensities ratios I_γ/I_α	Coefficients ratio R_γ/R_α	Quantity of each phase C_γ and C_α	
			C_γ (%)	C_α (%)
Non-annealing	0.042	0.693	6	94
Annealing: 1 h—500 °C	0.5125	1.25	41	59
Annealing: 1 h—600 °C	0.7015	1.43	49	51

Table 5
Values of crystal size for α and γ phases.

Specimens	Peaks (hkl)	FWHM B (rad)	Crystal size D (nm)
Non-annealed	(111) γ	0.0197	9
	(110) α	0.0096	17
Annealed	(111) γ	0.0042	40
1 h—500 °C	(110) α	0.0048	35
Annealed	(111) γ	0.0043	39
1 h—600 °C	(110) α	0.0053	32

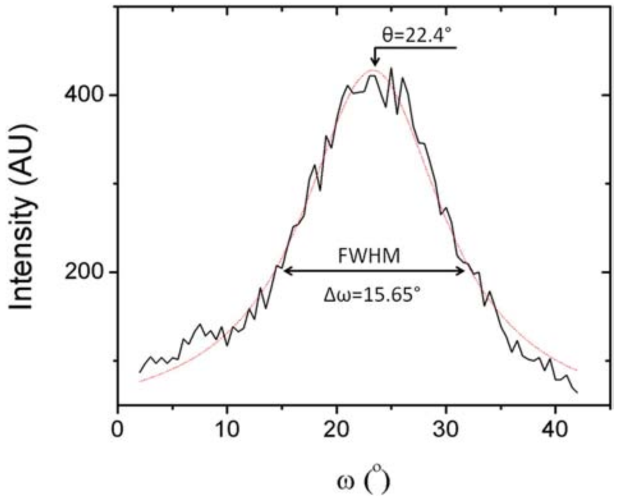

Fig. 5. Plot of the Ω-scan for the rocking curve peak of the (110) line of α- phase which is the majority in the annealed 304 stainless steel thin films. Solid line is the experimental curve, while dashed line is the Lorentzian fit curve.

annealed thin films, where the FWHM corresponds to the variation of Ω (ΔΩ). Since ΔΩ is relatively large, it indicates small disorientation of crystals with respect to the normal at the surface of the annealed thin film (OZ-axis). Therefore, the annealed thin films do not exhibit a preferential orientation of crystals, and α-phase grains are randomly distributed in thin film which can be considered as non-textured. The absence of texture has been also observed for all thin films regardless of their thicknesses, which might be due to the ultra-fine structure of thin films. In addition, annealing does not modify the texture of the initial α-phase, but it may influence the texture of the newly developed γ-phase that grows during annealing.

3.2.3. Residual stress

In a previous work, the residual stress was measured using the $\sin^2\psi$ method of XRD for as-grown 304 stainless steel thin films, where they were found to exhibit low tensile stress [17]. The $\sin^2\psi$ method ignores the thickness effect on stress due to their low thickness and since the penetration depth of X-ray is undefined [26]. In addition, the $\sin^2\psi$ method was used to estimate the stress of the majority α-phase. In contrary, the curvature method can be used to determine the stress of the mixture of α and γ phases for 304 stainless steel thin films. Herein, the curvature method may be used to study the influence of thin film thickness on residual stress value, because Stoney's relation takes into account the ratio H_s/h_f. In addition, the curvature method can also be used to study annealing effect on residual stress developed in the 304 stainless steel thin films.

When the stress (σ) is isotropic along the surface of a thin film, it imposes a curvature defined by the radius (R) on the substrate. Figure 6 demonstrates two curvature directions for silicon substrates and the types of stresses that correspond to them. Uncoated silicon substrate exhibits a pseudo-flat shape with a curvature radius (R_0), as shown in Fig. 6(a). In contrary, Fig. 6(b) reveals that coated silicon substrate contains tensile stress which tends to contract the film. In this case, silicon substrate exhibits a concave curvature shape described by σ(+). Nevertheless, Fig. 6(c) shows coated silicon substrate with a compressive stress which tends to extend the thin film. Herein, silicon substrate takes a convex curvature shape described by σ(−). It should be noted here that the curvature method considers the elasticity of silicon substrate, but it ignores the elasticity of the thin film.

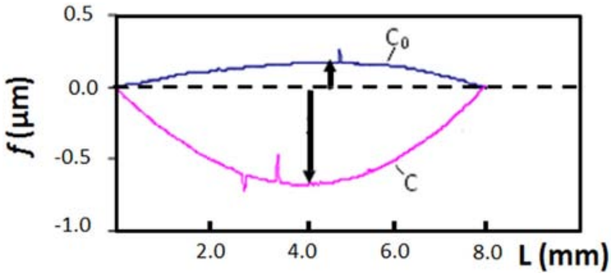

Fig. 7. The bend of silicon substrates: uncoated (C_0), and coated (C) as a function of substrate length (L). Thin film thickness is 120 nm (sample number 2 in Table 7). The sizes of the bowing are measured at the locations of the arrows.

Figure 7 shows the two curvatures C_0 and C which correspond to the curvatures of the uncoated and coated silicon substrates, respectively. They are obtained by mechanically sliding of stylus along of length of the substrate. The thickness of the presented thin film is 120 nm. The uncoated substrate exhibits low convex curvature while the coated substrate exhibits high concave curvature. f value of each curve in the figure can be used to calculate the curvature radius by Eq. (1), then the residual stress can be calculated using Eq. (2). The measured bowing values are estimated with a systematic error of ~5% due to the holder of the mechanical profilometer. The calculated stress and curvature radii of the substrates coated with thin films with different thicknesses are shown in Table 6, R_1 and σ_1 are before annealing while R_2 and σ_2 are after annealing.

The results presented in Table 6 reveal that the residual stresses developed in the 304 stainless steel thin films are tensile stresses (+σ), i.e. concave curvature of the substrates. The stress level does not depend on the thin film thickness, i.e. $\sigma_1 = +1.12 \pm 0.04$ GPa in average. This is due to the low thickness of the films (nanometer scale).

It is well established that residual stress is associated to defect density in crystal lattice [32]. In addition, the broadening of XRD peaks is caused mainly by the increase in defect density and residual stress of the material. Thus, the low tensile stress of the present thin films demonstrates that the grains of those thin film contains low concentration of defects.

Small disruption of the crystal lattice is responsible for the development of elastic stress field that corresponds to $\sigma_1 = +1.12 \pm 0.04$ GPa. In addition, small difference can be observed when comparing the current average stress value with that calculated using the $\sin^2\psi$ method for similar thin films ($\sigma = +1.7$ GPa) [17]. This difference can be attributed to the fact that the $\sin^2\psi$ method determines the stress only for the majority α-phase. However, the curvature method allows stress measurement of both α and γ phases. Therefore, the small difference in stress values can be assigned to the minority γ-phase that causes diminishing the stress of thin films.

Table 6 also shows that stress level is greatly reduced after annealing thin films ($\sigma_2 = +0.0005$ GPa). Thus, it can be concluded that annealing of a stainless steel thin film increases the relaxation of the thin film due

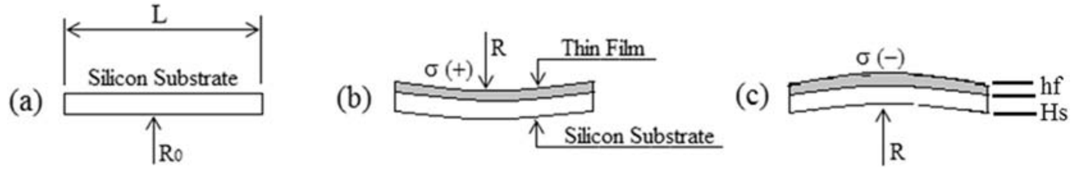

Fig. 6. Schematic representation for three types of curvatures for silicon substrates with different stress types: (a) uncoated silicon substrate, (b) coated silicon substrate under tensile stress (concave curvature), and (c) coated silicon under compressive stress (convex curvature).

Table 6
Calculated values of curve radius, and stress level by mean of curvature method.

Silicon substrate	No	Thin film thickness h_f (nm)	As-grown		Annealed	
			$(1/R_1)-(1/R_0)$ (10^{-7} mm)	σ_1 (GPa)	$(1/R_2)-(1/R_0)$ (10^{-7} mm)	σ_2 (GPa)
	1	110	+1057.25	+ 1.15	–	–
$H_s = 200$ μm	2	120	+1063.75	+1.06	–	–
	3	133	+1287.35	+1.16	–	–
L = 8 mm	4	166	+1544.50	+1.12	+0.625	+0.0005

to self-diffusion of atoms in the crystal lattice of α-phase caused by thermal agitation of atoms initiated by the increase in temperature. These processes are similar to the restoration process [33] or thermally activated process [34] where the diminish of defects eliminates elastic stress field in crystal lattice. In addition, those results suggest that γ-phase grains grow in the mixture structure of α and γ phases with minimal defects.

3.2.4. CEMS analysis

Figure 8 shows the CEMS spectra measured at room temperature for 304 stainless steel thin films: (a) as-grown, and (b) annealed at 600 °C. The CEMS spectrum of as-grown thin film reveals a paramagnetic singlet line at the center of the spectrum and ferromagnetic sextuplet composed of six wide lines. The ferromagnetic and paramagnetic components confirm the presence of α (ferromagnetic) and γ (paramagnetic) phases. The paramagnetic singlet line at the center of the spectrum (indicated by O in both spectra) corresponds to γ-phase, and the ferromagnetic sextuplet lines correspond to α-phase [17]. Deconvolution of the CEMS spectrum in Fig. 8(a) demonstrates that the first environment site (S1) is strongly ferromagnetic which belongs to α-phase which is rich in Cr. Hence, the second environment site (S2) is feebly ferromagnetic that also belongs to α-phase, and it is rich in Ni and Mn. The CEMS spectrum obtained for annealed thin films can be decomposed into two ferromagnetic sub-spectra sextuplet noted by S1 and S2, and paramagnetic single central line of γ-phase indicated by O. Figure 8(b) reveals that the intensity of the single central line that corresponds to the paramagnetic γ-phase increases while of the intensity of the sextuplet that corresponds to α-phase decreases significantly which confirms the α → γ transformation. In addition, the intensity modification of the spectrum is caused by the increase in the quantity of γ -phase due to phase transformation and the intensity of α-phase [35]. These results are in agreement with previous work performed for stainless steel thin films fabricated by sputtering and reveal that the 600 °C belongs to the temperatures range that correspond to the phases transformation [15]. Figure 8(b) also reveals an interesting feature where the ferromagnetic contribution of the spectrum is divided into two sub-spectra sextuplets which indicates the presence of two ferromagnetic sites of Fe that are not equivalent.

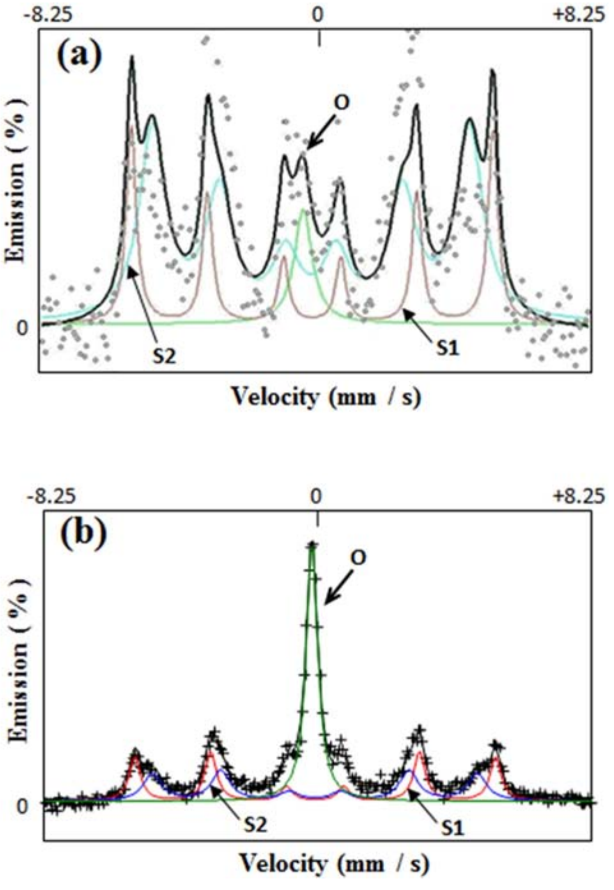

Fig. 8. CEMS spectra obtained at room temperature for non-annealed (A) and annealed at 600 °C (B) 304 stainless steel thin films on quartz substrates. In this figure, the single central paramagnetic line is indicated by the letter "O".

The Mössbauer parameters obtained from the single central line and the two ferromagnetic sextuplets of deconvoluted CEMS spectrum are shown in Table 7. The table shows that the single central line of γ-phase has an isomeric shift of the annealed (A) film is IS = −0.08 mm/s with a relative area of 37.4%. Whereas, the external S1 and the internal S2 sextuplets of ferromagnetic spectra have average hyperfine magnetic fields of $H_{1(A)} = 33.8$ T and $H_{2(A)} = 30.4$ T with the relative areas of $A_1 = 31.4\%$ and $A_2 = 30.4\%$.

Unlike the previous work [36], it was shown that the CEMS spectrum of as-grown (NA) thin films exhibits a single central line that corresponds to γ-phase with isomeric shift of IS = −0.14 mm/s and a relative area of 11%. The average hyperfine magnetic fields that correspond to the S1 and S2 sextuplets of magnetic spectrum are $H_{1(NA)} = 33.4$ T and $H_{2(NA)} = 27.5$ T with relative areas of $A_1 = 59\%$ and $A_2 = 30\%$. Those results reveal that $H_{1(A)}$ of annealed thin films is slightly higher than that of as-grown thin films $H_{1(NA)}$. $H_{1(A)}$ corresponds to the average hyperfine field of bulk alloy of $Fe_{90}Ni_{10}$ composition [37] which indicates that S1 is more rich in Ni of annealed thin films than the as-grown. For the internal S2 sextuplet, $H_{2(A)}$ of annealed thin films is significantly larger than that of $H_{2(NA)}$ of non-annealed thin films. $H_{2(A)}$ corresponds to the average hyperfine field for bulk alloy of $Fe_{89}Cr_{11}$ composition [38], which indicates that S2 is more poor in Cr for annealed thin films compared with non-annealed thin films. This indicates that annealing of the thin films at 600 °C for 1 h causes the Cr rich precipitates to be formed between crystals, causing the depletion of Cr in the crystal center [39–41]. These phenomena have been also observed for stainless steel thin films prepared by ion beam deposition and annealed at temperatures higher than 500 °C [10]. Table 7 also reveals that both isometric shifts values are for annealed and as-grown thin films are close to zero. In addition, annealing thin films led to a slight decrease of the angle, here $\theta_{(A)} = 73°$ and $\theta_{(NA)} = 78°$. This indicates that the direction of the average magnetic moment is slightly deflected due to annealing effect.

Table 7
Parameters of CEMS sub-spectra.

304 SS thin films	Sub-spectra	Magnetic hyperfine field (T)	Angle ‘θ’ (°)	Isomeric shift IS (mm/s)	Relative area A (%)
Non-annealed	External Sextuplet (S1)	33.4	78	0.03	59
	Internal Sextuplet (S2)	27.5	78	−0.007	30
	Central single line (paramagnetic)	–	–	−0.14	11
Annealed 1 h −600 °C	External Sextuplet (S1)	33.8	73	0.01	31.4
	Internal Sextuplet (S2)	30.4	73	~0	31.1
	Central single line (paramagnetic)	–	–	−0.08	37.4

4. Conclusion

Stainless steel thin films were fabricated by thermal evaporation on quartz substrates and annealed under ultra-high vacuum at 500 °C and 600 °C for 1 h at each temperature. Conversion electron Mössbauer spectroscopy and X-ray diffraction analyses revealed the presence of both phases of stainless steel: α-phase of body-centered cubic structure (BCC), and γ-phase of face-centered cubic (FCC). Annealing of 304 stainless steel thin films ensures the α → γ transformation of the structure and causes reduction of disruption in crystal lattice of α, and the growth of a new γ-phase with minimal defects. Crystal sizes of annealed thin films for α and γ phases are almost identical. The development in crystal size of both phases with annealing could be described by heterogeneous germination, where the germination rates of α and γ crystals, are inversely proportional. X-ray diffraction rocking curve method was used to determine the texture degree of the thin films and it showed that annealed thin films do not exhibit a preferential orientation of crystals. The stress of as-grown thin films was found to be independent on the thin film thickness, and it is equal to +1.12 ± 0.04 GPa in average as determined by the curvature method. Nevertheless, the stress of the thin films was reduced after annealing to +0.0005 GPa due to relaxation of the thin films that was caused by reduction of disruption initiated by self-diffusion of atoms in the crystal lattice. Overall, the present study introduces a procedure for α → γ phase transformation of stainless steel thin films, produced by thermal evaporation, that might be utilized for practical applications including, but not limited to, medical production, chemical processing, food production, oil and gas, and power generation.

References

[1] R.M. Fernández-Domene, E. Blasco-Tamarit, D.M. García-García, J. García-Antón, Effect of alloying elements on the electronic properties of thin passive films formed on carbon steel, ferritic and austenitic stainless steels in a highly concentrated LiBr solution, Thin Solid Films 558 (2014) 252–258.

[2] T. Li, L. Liu, B. Zhang, Y. Li, X. Wang, F. Wang, Direct observation of thin membrane passive film over the growing pit on sputtered nanocrystalline austenitic stainless steel film, Electrochem. Commun. 52 (2015) 80–84.

[3] S. Cao, B. Liu, L. Fan, Z. Yue, B. Liu, B. Cao, Highly antibacterial activity of N-doped TiO_2 thin films coated on stainless steel brackets under visible light irradiation, Appl. Surf. Sci. 309 (2014) 119–127.

[4] T.C.K. Yang, Y.-L. Yang, R.-C. Juang, T.-W. Chiu, C.-C. Chen, The novel preparation method of high-performance thermochromic vanadium dioxide thin films by thermal oxidation of vanadium-stainless steel co-sputtered films, Vacuum (2015), http://dx.doi.org/10.1016/j.vacuum.2015.1005.1001.

[5] K. Nomura, T. Okubo, M. Nakazawa, Surface analysis of thin stainless steel films and thick-coated steel by simultaneous application of conversion electron and X-ray Mössbauer spectroscopy, Spectrochim. Acta B At. Spectrosc. 59 (2004) 1259–1264.

[6] G. Fu, N.H. Loh, S.B. Tor, B.Y. Tay, Y. Murakoshi, R. Maeda, Injection molding, debinding and sintering of 316L stainless steel microstructures, Appl. Phys. A Mater. Sci. Process. 81 (2005) 495–500.

[7] J. Barralis, G. Maeder, Précis de métallurgie: élaboration, structures-propriétés et normalisation, fourth ed. AFNOR: Nathan, Paris, 1988.

[8] R.-C. Juang, Y.-C. Yeh, B.-H. Chang, W.-C. Chen, T.-W. Chung, Preparation of solar selective absorbing coatings by magnetron sputtering from a single stainless steel target, Thin Solid Films 518 (2010) 5501–5504.

[9] C. Lee, J. Bae, Oxidation-resistant thin film coating on ferritic stainless steel by sputtering for solid oxide fuel cells, Thin Solid Films 516 (2008) 6432–6437.

[10] J.P. Eymery, G. Laplanche, M. Cahoreau, M.F. Denanot, Structural investigation of b.c.c. 304 stainless steel, Thin Solid Films 217 (1992) 1–6.

[11] S.D. Dahlgren, Equilibrium phases in 304L stainless steel obtained by sputter-deposition, Metall. Trans. 1 (1970) 3095.

[12] P.J. Grundy, J.M. Marsh, Amorphous thin films of stainless steel, J. Mater. Sci. Lett. 13 (1978) 677–681.

[13] J.P. Eymery, G. Laplanche, Structural and magnetic study of bcc 304 stainless steel thin films elaborated by ion sputtering, J. Magn. Magn. Mater. 93 (1991) 179–182.

[14] K.H. Behrndt, Formation of amorphous films, J. Vac. Sci. Technol. 7 (1970) 385–398.

[15] J.P. Eymery, R. Krishnan, On some magnetic properties of 304 stainless steel films, J. Magn. Magn. Mater. 104–107 (1992) 1785–1786.

[16] C.B. Post, W.S. Eberly, Stability of austenite in stainless steels, Trans. ASM 39 (1947) 868.

[17] N. Merakeb, A. Messai, A. Djelloul, Ahmad I. Ayesh, Structural, mechanical, and magnetic properties of ferrite–austenite mixture in evaporated 304 stainless steel thin films, Appl. Phys. Mater. Sci. Process. 121 (2015) 739–748.

[18] L. Holland, Vacuum Deposition of Thin Films, sixth ed. Chapman and Hall Ltd., UK, 1966.

[19] C. Li, D. Cui, Y. Zhou, H. Lu, Z. Chen, D. Zhang, F. Wu, Asymmetric rocking curve study of the crystal structure orientations for $BaTiO_3$ thin films grown by pulsed laser deposition, Appl. Surf. Sci. 136 (1998) 173–177.

[20] T.N. Blanton, M. Lelental, C.L. Barnes, The use of X-ray diffraction rocking curve methodology for assessment of the c-axis orientation in BiSrCaCuO superconducting thin films, Phys. C 184 (1991) 119–126.

[21] S.W. Wilkins, Bragg-case X-ray thin-crystal rocking curves for Si — a direct comparison between theory and experiment, Phys. Lett. A 66 (1978) 134–136.

[22] B. Boubeker, M. Talea, P. Goudeau, C. Coupeau, J. Grilhe, On the Young's modulus of 304L stainless steel thin films, Mater. Charact. 45 (2000) 33–37.

[23] G.C.A.M. Janssen, M.M. Abdalla, F. van Keulen, B.R. Pujada, B. van Venrooy, Celebrating the 100th anniversary of the Stoney equation for film stress: developments from polycrystalline steel strips to single crystal silicon wafers, Thin Solid Films 517 (2009) 1858–1867.

[24] G.G. Stoney, The tension of metallic films deposited by electrolysis, Proc. R. Soc. Lond. A 82 (1909) 172.

[25] S. Dushman, Scientific Fondations of Vacuum Techniques, first ed. John Wiley, London, 1949.

[26] B.D. Cullity, Elements of X-ray Diffraction, second ed. Addison-Wesley Pub. Co., 1978 Reading, Mass.

[27] F.S. Li, J.J. Sun, C.L. Chien, Fe-57 Mossbauer study of metastable-304 stainless-steel film with, BCC structure, J. Phys. Condens. Matter 7 (1995) 1921–1931.

[28] B.L. Averbach, M. Cohen, X-ray determination of retained austinite by integrated intensities, Trans. AIME 176 (1948) 401.

[29] M.J. Godbole, A.J. Pedraza, L.F. Allard, G. Geesey, Characterization of sputter-deposited 316L stainless steel films, J. Mater. Sci. 27 (1992) 5585–5590.

[30] W.A. Jonhson, R.F. Mehl, Reaction kinetics in processing of nucleation and growth, Trans. AIME 135 (1939) 416–458.

[31] I. Vincze, I.A. Campbell, A.J. Meyer, Hyperfine field and magnetic moments in b.c.c. Fe–Co and Fe–Ni, Solid State Commun. 15 (1974) 1495–1499.

[32] S. Murugesan, P. Kuppusami, E. Mohandas, M. Vijayalakshmi, X-ray diffraction Rietveld analysis of cold worked austenitic stainless steel, Mater. Lett. 67 (2012) 173–176.

[33] R.E. Reed-Hill, Physical Metallurgy Principles, PWS Engineering Ltd, UK, 1973.

[34] C. Barrett, T. Massalski, Structure of Metals, Crystallographic Methods, Principles and Data (International Series on Materials Science and Technology), third ed. 1986, p. 398.

[35] T.W. Barbee, B.E. Jacobson, D.L. Keith, Microstructure of amorphous 304 stainless steel-carbon alloys synthesized by magnetron sputter deposition, Thin Solid Films 63 (1979) 143–150.

[36] N. Merakeb, J.-P. Eymeryb, A. Fnidikic, P. Goudeaub, B. Bouzabata, Evidence for two ferromagnetic iron sites in Fe–Cr–Ni thin films prepared by thermal evaporation, Mater. Lett. 58 (2004) 711–715.

[37] I. Vincze, I.A. Campbell, Mössbauer measurements in iron based alloys with transition metals, J. Phys. F: Met. Phys. 3 (1973) 647–663.

[38] S.M. Dubiel, J. Zukrowski, Mössbauer effect study of charge and spin transfer in Fe–Cr, J. Magn. Magn. Mater. 23 (1981) 214–228.

[39] S.R. Ortner, A stem study of the effect of precipitation on grain boundary chemistry in AISI 304 steel, Acta Metall. Mater. 39 (1991) 341–350.

[40] A. Guinier, Precipitation phenomena in supersaturated solid solution, Trans. AIME 206 (1956) 673.

[41] D. Séférian, P. Chevenard, Metallurgie de la Soudure nouveau Tirage, Dunod, Edité par Paris, 1965.